

Imaging and integral field spectroscopy of shocked H₂ around G25.65+1.05

Stephen P. Todd^{1,2*} and Suzanne K. Ramsay Howat^{1†}

¹UK Astronomy Technology Centre, Royal Observatory, Blackford Hill, EH9 3HJ, UK.

²Institute of Astronomy, University of Edinburgh, Royal Observatory, Blackford Hill, EH9 3HJ, UK.

Accepted . Received ; in original form

ABSTRACT

Near-infrared imaging of the emission from molecular hydrogen is a powerful method for discovering outflows in star-forming regions. We present new near-infrared images, long slit and integral field spectroscopy of the ultra-compact H II region G25.65+1.05. These new observations reveal shocked H₂ emission associated with a bipolar outflow from a young high mass star at the centre of the source. The physical parameters of the outflow are discussed and compared with outflows from lower mass stars.

Key words: Objects: G25.65+1.05; star-formation: young stellar objects; star-formation: high mass stars

1 INTRODUCTION

A number of recent surveys have invigorated the study of high mass star formation by providing data on coherent samples of candidate high mass young stellar objects (HMYSOs) (e.g. Palla et al. 1991, Molinari et al. 1996, Molinari et al. 1998, Ridge & Moore 2001, Sridharan et al. 2002). Until these surveys became available the relative scarcity of HMYSOs, the large distances to the closest examples (a few kpc) and the high extinction to these objects had limited their study to a few, well-known examples. Thus, there are many questions still remaining as to the nature of high-mass star formation, and the similarities and differences in high and low mass stellar evolution.

Outflows are associated with the formation of stars of all masses and are the subject of a number of the HMYSO surveys (Shepherd & Churchwell 1996b, Shepherd & Churchwell 1996a, Zhang et al. 2001). While the role of outflows in the formation of low-mass stars is comparatively well studied (see for example the review by Richer et al. 2000), far less is known about the properties and role of outflows associated with the formation of high-mass stars (M greater than $\sim 8 M_{\odot}$). A radio survey of molecular line emission from high-mass star forming regions showed that high-velocity molecular gas (CO) is associated with around 90% of these regions (Shepherd & Churchwell 1996a). Two sources (G25.65+1.05 and G240.31+0.07) were mapped at higher spatial resolution and found to have bi-

lar outflows. In a follow-up survey, Shepherd & Churchwell (1996b) mapped a further ten of the best candidates for having bipolar molecular outflows and confirmed the presence of such an outflow in 5 of those sources. Zhang et al. 2001 observed 69 candidate high mass protostars in the CO J=2-1 transition and argue that as many as 90% of the sources may have outflows. Beuther et al. (2002a), mapping at a higher spatial resolution, found evidence of bipolar outflows in 21 of their 26 sources suggesting that bipolar outflows may be associated with most young high mass stars. The first report of molecular hydrogen line emission associated with high mass star formation was from Lee et al. (2001), following up a search for the near-infrared counterparts of ultra-compact H II regions by Walsh et al. (1999). Lee et al. (2001) found evidence for outflows in IRAS 15278-5620 and IRAS 16076-5134.

These surveys confirm the importance of outflows for HMYSO evolution. Further work is required to determine whether the physics of the HMYSO outflows is the same as for low mass YSOs. The observed outflows appear to have much lower collimation factor – between 1 and 1.8 – than those seen from low-mass stars which often have a collimation factor of around 10 (see, for example, the interferometric observations of Richer et al. (2000)). This would be hard to explain if the outflows are formed by the same jet entrainment model as that believed to describe the outflows from low-mass stars. However, Beuther et al. (2002a) argued that the observed degree of collimation could be significantly reduced by the low spatial resolution of the maps, which could be consistent with well collimated high-mass flows. Interferometric observations have shown collimation

* E-mail: spt@roe.ac.uk (SPT)

† E-mail: skr@roe.ac.uk (SKRH)

factors as high as 10 (Beuther et al. 2002b) in flows from high-mass stars and have revealed that some of these apparently uncollimated flows can be resolved into several well collimated flows from separate young stars. Detection of multiple flows in a region in which high-mass stars are forming would not be surprising. High-mass stars are known to form in dense clusters (Garay & Lizano 1999), so high spatial resolution observations are essential for identifying the source of an individual outflow. The presence of a collimated outflow would imply the presence of a stable accretion disk and hence strengthen the view that high mass stars are formed by steady accretion, in a similar way to low mass stars, rather than by merging of intermediate-mass protostars in the centre of dense clusters.

We have embarked upon a near-infrared survey of HMYSOs, which will be presented in full in Varricatt et al. (2005, in preparation). The survey is designed to reveal outflows by mapping at sub-arcsecond spatial resolution in the $v=1-0$ S(1) line of molecular hydrogen. NIR observations of H_2 have frequently been used to study outflows from low mass YSOs. In this paper we present near-IR imaging, integral-field and long-slit spectroscopic observations of new outflows in the region of the ultra-compact H II region G25.65+1.05.

G25.65+1.05 (also IRAS 18316–0602 or RAFGL7009S) is an irregular, compact radio source, first identified at 3.6cm by Kurtz et al. (1994). It is located at a distance of 3.2kpc (Molinari et al. 1996). The radio peak is coincident with an unresolved infrared source, identified as a young B1V star with a large K-band excess (Zavagno et al. 2002) and is also closely associated with methanol (Molinari et al. 1996) and ammonia maser emission (Walsh et al. 2003, Szymczak et al. 2000). Submillimetre continuum observations at 350 μ m (Hunter et al. 2000), 450 μ m and 850 μ m (Walsh et al. 2003) are all peaked at the position of the radio and maser sources. Observation of the CS (2-1) line by Bronfman et al. (1996) shows an excellent match of the observed radial velocity from the masers (40.8–42.4 $km\ s^{-1}$, Walsh et al. 2003) and the line emission (41.4 $km\ s^{-1}$) indicating a strong link between the dense gas, the maser sources and the massive star. Zavagno et al. 2002 propose that one explanation for the observed *K*-band excess from the central source may be the presence of a disk. ISO spectroscopy of this source shows a rich spectrum of ice features including absorption features attributed to H_2O , CH_3OH , CO_2 , $^{13}CO_2$, CO , OCS , $HCOOH$, $HCOO^-$, CH_3HCO , CH_4 , NH_3 and Silicate (see Gibb et al. 2004 and references therein). Laboratory spectra fitted to the ISO observations suggests that the ice features arise in dense material with temperatures in the range 10K–100K.

2 OBSERVATIONS

2.1 Imaging

Imaging observations were made on 29 June 2002 using the facility infrared imager, UFTI (Roche et al. 2003), at the UK Infrared Telescope (UKIRT). UFTI is a 1 to 2.5 μ m camera using a 1024 \times 1024 HgCdTe array with a plate scale of 0.091 arcsec/pixel. A single 9-point jitter in a 3 \times 3 pattern with offsets of 10 arcsec was observed with 60 sec exposures

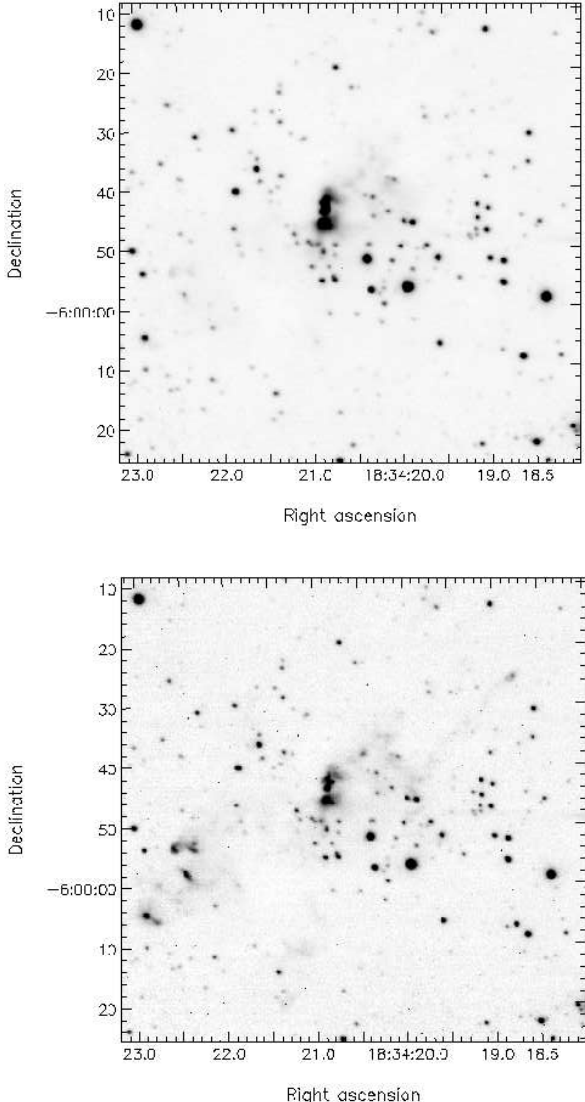


Figure 1. Part of the UFTI mosaic images (a) K98 broad-band filter; (b) 1–0 S(1) narrow-band filter. All coordinates are J2000.

using the *K*98 broad-band filter, giving 9 min on source. The same 9-point jitter pattern was repeated three times using exposures of 100 s with the 2.122 μ m 1 – 0 S(1) H_2 narrow-band filter giving a total of 45 min on source. The individual frames from each filter were flat-fielded and mosaiced together automatically by the ORAC-DR pipeline.

Sources emitting in the H_2 line will be detected in both the broad-band and narrow-band images but will appear brighter relative to the continuum sources in the narrow-band images. The two mosaics are shown in Figure 1. The narrow-band image with 0.6 arcsec seeing was smoothed to match the 0.7 arcsec seeing of the broad-band image. The broad-band image was scaled in intensity using the flux from the field stars and subtracted from the narrow-band image to leave the H_2 emission as shown in Figure 2. The H II region itself and some stars around it appear negative in this subtracted image due to differential extinction to the core compared with the field stars used for flux scaling. The

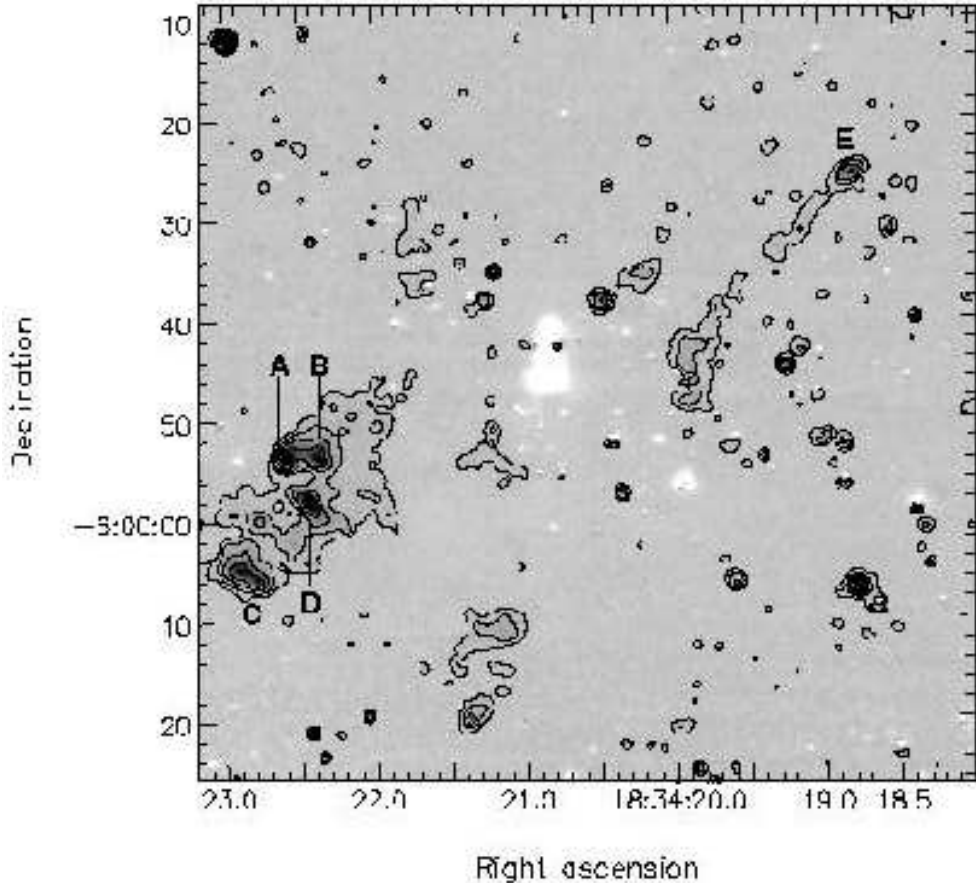


Figure 2. A continuum subtracted 1–0 S(1) image created by subtracting Figure 1a from Figure 1b. The contours are drawn from a version of the image smoothed with a 0.5 arcsec gaussian and are logarithmically spaced with each contour a factor of two higher in flux than the previous one from an arbitrary lowest contour. All coordinates are J2000.

increased reddening makes it relatively brighter in the broad-band image. A number of point sources are visible in addition to the extended emission. These are ghost images of bright stars produced by the narrow-band filter and residuals left where stars have been imperfectly subtracted. The complete mosaic covers a 1.8×1.8 arcmin field centred on the H II region. No H₂ emission was detected outside the region shown here. The brightest H₂ emission was detected to the south-east of the H II region, taking the form of a region of faint, diffuse emission containing a number of bright, compact sources (A–D). To the north-west of the H II region there is a straight, narrow line of faint emission with a bright source (E) at one end. There is also faint, diffuse emission to the south and north-east of the H II region.

2.2 Long-slit spectroscopy

Long slit spectra of sources C and D were obtained on 30 June 2002 at UKIRT using Cooled Grating Spectrometer 4 (Mountain et al. 1990). The 40 l/mm grating was used, giving a wavelength coverage of 1.9 to 2.5 μm and the sources were observed with a single slit position. A one pixel (0.6 arcsec) wide slit was used and the detector was stepped over 2 pixels in half-pixel increments to give a fully sampled spectrum with a spectral resolution of 600. Observations were

made through thick, patchy cirrus causing large variations in the detected flux. Individual exposures were weighted by the square of the signal to noise ratio of the $v = 1 - 0$ S(1) line before they were added together to maximise the signal to noise ratio of the combined data. The spectrum was ratioed by a standard star with its blackbody shape corrected, to remove atmospheric telluric features. The final spectra of the two sources are shown in Figure 3.

2.3 Integral field spectroscopy

Sources A and B were observed on 24 October 2002 as part of the UIST commissioning observations. UIST is a new facility class near-IR (1–5 μm) imager and spectrometer at UKIRT which uses a 1024×1024 InSb array (Ramsay Howat et al. 2000). It includes a deployable cryogenic image-slicing IFU with 14 slices, each 0.24 arcsec wide. The pixel scale along the slices is 0.12 arcsec/pixel resulting in a field of view of $3.36 \text{ arcsec} \times 5.52 \text{ arcsec}$, which can be rotated to any angle on the sky. The HK grism was used, giving a spectral coverage of 1.4–2.5 μm with a spectral resolution of 800–1000.

The target was acquired using UIST in *K*-band imaging mode. The IFU field of view was rotated to a position angle of 90° , making the long axis of the field run E–W. Two

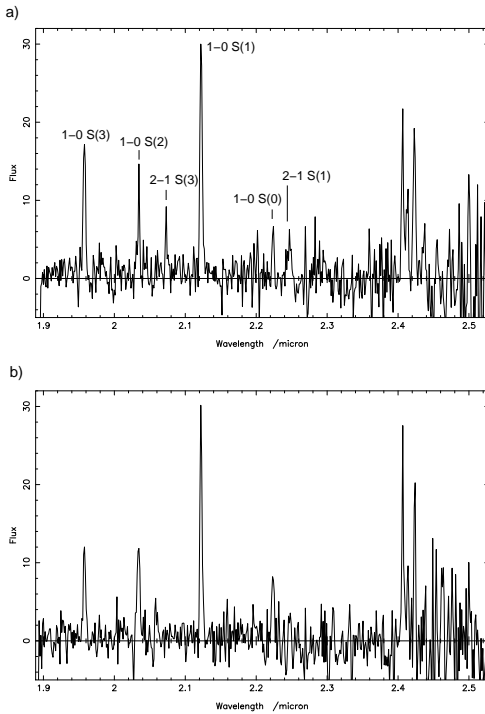


Figure 3. CGS4 long-slit spectra of a) source C and b) source D. The flux is in arbitrary units.

adjustments to the pointing were made during the observations (1 arcsec E, then 1 arcsec S). A total of three positions were observed for 8mins each giving a maximum integration of 24mins on-source for the overlap region. Sky frames were obtained by offsetting to a separate sky position. The standard star BS7260 was observed to provide correction for telluric atmospheric features and flux calibration.

2.3.1 Combining the data into a single datacube

The observations at each of the three positions described above were formed into an (x, y, λ) data-cube using the ORAC-DR pipeline employed for all on-line data reduction at UKIRT. Each frame was divided by a flat-field frame. Sky-subtracted frames were wavelength calibrated using a spectrum of an argon arc lamp and the resulting frames formed into a datacube. All of the spectra in the datacube were divided by the standard-star spectrum, corrected for the black-body shape of the stellar continuum, to remove variations in atmospheric transmission. An approximate flux calibration was obtained using the magnitude of the star ($K=4.48$). The IFU data reduction pipeline is described in more detail in Todd et al. (2002).

The known 1 arcsec telescope offsets were used to register the three data-cubes in the two spatial dimensions. These were mosaiced into a single data-cube using MAKE-MOS, which is included in the Starlink CCDPACK package. An image extracted from this datacube at the wavelength of the $v = 1 - 0$ S(1) H_2 line ($2.122 \mu\text{m}$) is shown in Figure 4. A spectrum of the sum of the brightest part of source A is shown in Figure 5. All detected emission lines are from H_2 .

A spectrum was formed by summing over all spatial pixels of the data-cube. A Gaussian profile was fitted to the

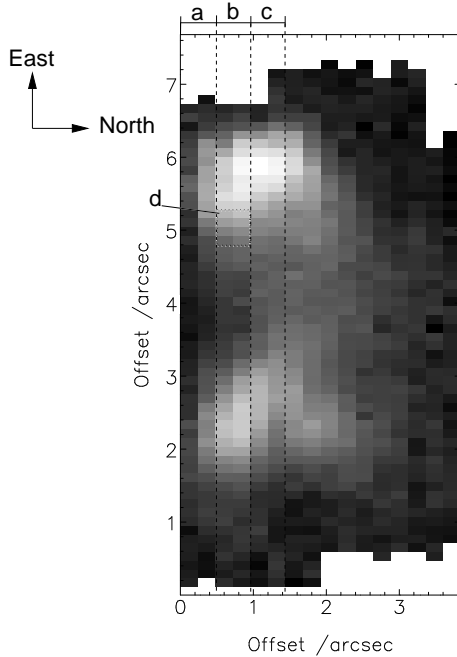


Figure 4. The spectral line image of sources A and B at the wavelength of the $1 - 0$ S(1) line, extracted from the IFU datacube. The offsets are arbitrary and from the edge of the IFU field, which was centred on $\alpha = 18^{\text{h}}34^{\text{m}}23.5^{\text{s}}$, $\delta = -6^{\circ}53'00''$. At a distance of 3kpc, 1arcsec corresponds to 0.015pc.

bright $1 - 0$ S(1) line in this spectrum and was found to be centred at $(2.12209 \pm 0.00003) \mu\text{m}$ with FWHM $(2.28 \pm 0.05) \times 10^{-3} \mu\text{m}$. The other lines are all much weaker, so to obtain the best possible measurement of the flux in each line a Gaussian profile was scaled to fit the line keeping the FWHM of the line fixed at $0.00228 \mu\text{m}$ and the offset of the line from the $1 - 0$ S(1) line fixed by the known wavelength of the line. In total, 12 lines from the $v=1$ and $v=2$ transitions were detected. The measured fluxes are reported in Table 1.

3 RESULTS AND DISCUSSION

3.1 Morphology

The K-band image of G25.65+1.05 (Figure 1a) is dominated by the nebulous continuum emission surrounding the central, unresolved, source at $\alpha = 18^{\text{h}}34^{\text{m}}20.9^{\text{s}}$, $\delta = -6^{\circ}02'42.3''$ seen by Zavagno et al. (2002). The morphology of the H_2 emission in Figure 4 is strongly suggestive of a moderately well-collimated outflow, or outflows, centred on G25.65+1.05. Sources A, B, C and D are connected by diffuse emission and appear to form one lobe of an outflow with a flow axis through G25.65+1.05 to source E. The outflow has a position angle on the sky of 130° East of North. This is consistent with the direction of the highly energetic bipolar outflow found to be centred on or close to the $H\text{ II}$ region by Shepherd & Churchwell (1996b). Sources ABCD are spatially co-incident with the blueshifted lobe seen in the CO outflow and E with the redshifted lobe. The relative faintness of E compared with ABCD may then be interpreted as being due to E being embedded further in the molecular cloud. The projected length of the outflow, taken

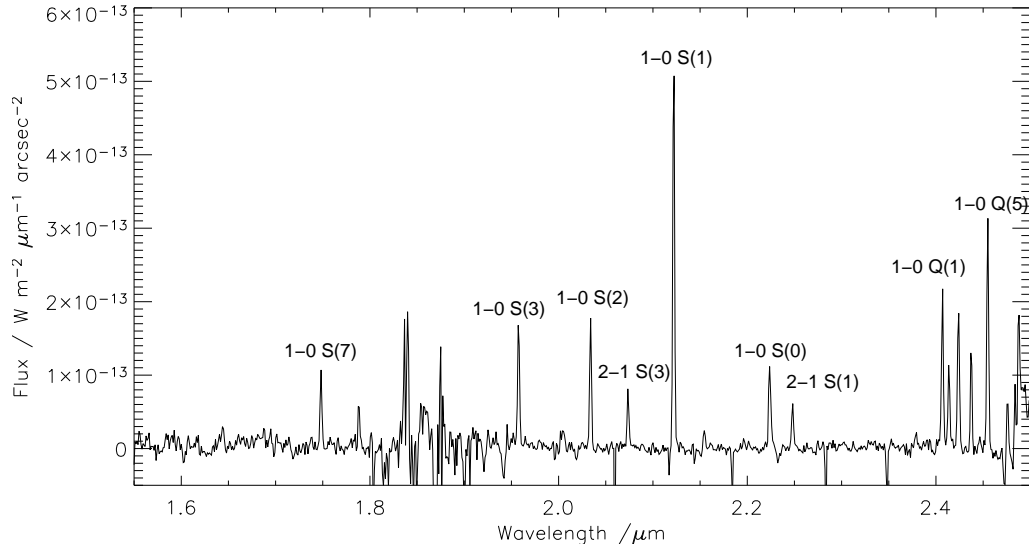


Figure 5. The spectrum obtained by summing over the brightest region of source A. Fluxes measured from this spectrum are given in Table 1.

Table 1. Measure fluxes and physical parameters for the lines measured.

Transition	λ_j / μm	E_j / K	A_j / 10^{-7} s	g_j	Flux / $\text{W m}^{-2} \text{arcsec}^{-2}$
1 – 0 S(7)	1.7480	12817	2.98	57	$(2.4 \pm 0.2) \times 10^{-16}$
1 – 0 S(3) †	1.9576	8365	4.21	33	
1 – 0 S(2)	2.0338	7584	3.98	9	$(4.4 \pm 0.2) \times 10^{-16}$
2 – 1 S(3)	2.0735	13890	5.77	33	$(1.7 \pm 0.2) \times 10^{-16}$
1 – 0 S(1)	2.1218	6956	3.47	21	$(11.4 \pm 0.2) \times 10^{-16}$
1 – 0 S(0)	2.2235	6471	2.53	5	$(2.7 \pm 0.2) \times 10^{-16}$
2 – 1 S(1)	2.2477	12550	4.98	21	$(1.7 \pm 0.2) \times 10^{-16}$
1 – 0 Q(1) †	2.4066	6149	4.29	9	
1 – 0 Q(2) †	2.4134	6471	3.03	5	
1 – 0 Q(3) †	2.4237	6956	2.78	21	
1 – 0 Q(4)	2.4375	7586	2.65	9	$(3.0 \pm 0.3) \times 10^{-16}$
1 – 0 Q(5) †	2.4548	8365	2.55	33	

The wavelengths, upper energy levels, Einstein A coefficients and degeneracies of the H₂ lines detected in our spectra. Lines marked † were found to be absorbed by unresolved atmospheric absorption features and were discarded. The fluxes given are measured from the spectrum in Figure 5 and are not corrected for extinction.

to be the distance from C to E, is ~ 70 arcsec. In the absence of any information, we assume an angle relative to the plane of the sky of 45° . This gives an estimate of the total length of 1.4 pc and a collimation factor ~ 3 . Interpreted as a single outflow, we find a lower degree of collimation than is seen in outflows from low-mass YSOs, but higher than the 1-1.8 often assumed for high-mass YSOs.

Shepherd & Churchwell (1996b) found two velocity components associated with G25.65+1.05 at 39 km s^{-1} and at 49 km s^{-1} . One possible interpretation of the H₂ emission in this region would be to see sources A and B as bow-shocks in a highly collimated flow from west to east, as suggested by their morphology. This would imply the presence of another, more deeply embedded source to the south and west of G25.65+1.05. The MSX point source catalogue (Egan et al.

1999) shows a single source associated with G25.65+1.05 ($\alpha = 18^\text{h}34^\text{m}21.2^\text{s}$, $\delta = -6^\circ02'36.96''$ with a positional accuracy of $4''$ – $5''$) so does not support an argument for a second source offset south-west of G25.65+1.05. Furthermore, a recent submillimetre survey by Hill et al. (2005) finds a single core of mass $1. \times 10^3 M_\odot$ associated with G25.65+1.05, located at the position of the methanol maser (Molinari et al. 1996), consistent with an earlier result by Faúndez et al. (2004).

In the following Section, the near-IR spectra of sources ABCD are analysed and shown to support our model of the emission arising due to a single outflow.

3.2 H₂ Excitation in the G25.65+1.05 Outflow

The near-infrared emission from H₂ can be produced either by thermal excitation in shock-fronts or fluorescent excitation by non-ionizing ultraviolet photons ($91.2 < \lambda < 110.8$ nm) from hot young stars. These cases may be distinguished using the near-IR spectrum, though the detection of lines from a broad range of energy levels is required to obtain a secure result. For shock-excited H₂, the lower energy levels ($v=1$) are typically populated as for a gas in local thermal equilibrium (LTE) with a characteristic excitation temperature of a few thousand Kelvin, though in reality the temperature of the cooling gas will vary over a range from a few hundred to a few thousand Kelvin. The emission lines would also be broadened to tens of km s⁻¹. This is less than our instrumental resolution and undetectable in the spectroscopy of G25.65+1.05.

For radiatively excited gas, the populations follow a non-LTE distribution, characterised by high excitation temperatures ($\sim 10,000$ K). Lines from high vibrational levels ($v > 1$) may be detected and the ratio of the intensity of the 1 – 0 S(1) line to that of the 2 – 1 S(1) H₂ line is ~ 2 if the density is low (Sternberg & Dalgarno 1989). For gas above the critical density ($n_{H_2} \sim 10^5$ cm⁻³), collisional de-excitation becomes important and the level populations tends towards an LTE population.

The spectra of G25.65+1.05 provide high signal/noise observations of lines from the $v=1$ and $v=2$ vibrational levels. Deeper observations would be required to obtain line strengths for the higher vibrational levels and thereby to confirm the excitation. However, there are indicators that the H₂ is shock excited which, taken in aggregate, lead us to conclude that this is indeed the case.

In the following sections, we obtain the excitation temperatures for the sources in G25.65+1.05. These are in the range 1000–3000 K indicative of thermal excitation. When molecular hydrogen is radiatively excited, 90% of the H₂ is dissociated by the ionizing photons ($\lambda < 91.2$ nm) that are also present. This may result in emission in the 2.166 μm Brackett- γ recombination line. The spectra of sources ABCD contain only emission lines of H₂. We note that the absence of Brackett- γ emission is not a strong constraint as some fluorescently excited photodissociation regions emit only H₂ lines. Finally we cite the bow-shock morphology seen clearly in Figure 4, perhaps the strongest indicator that the H₂ is excited by a shock front driven by an outflow rather than heated from within the knots by embedded point sources.

3.2.1 The Excitation Temperature of Sources A and B

The measured intensity, I , of a given H₂ line can be used to calculate the column density of the upper excitation level of the transition:

$$N_j = \frac{4\pi\lambda_j I}{A_j hc} \quad (1)$$

where A_j is the Einstein A -coefficient of the transition. The relative column densities of any two excitation levels can be expressed in terms of an excitation temperature T_{ex} :

$$\frac{N_i}{N_j} = \frac{g_i}{g_j} \exp\left(\frac{-(E_i - E_j)}{kT_{\text{ex}}}\right) \quad (2)$$

where g_j is the degeneracy and E_j is the energy of the level. The values of λ_j , E_j , A_j and g_j for the lines detected in our spectra are shown in Table 1.

Before we could use our measured intensities to derive the excitation temperature of the gas it was necessary to measure and compensate for extinction. In the absence of more information it was assumed that the extinction was constant across the IFU field of view. An extinction law of the form $\tau(\lambda) = A_k (\lambda/2.2\mu\text{m})^{-1.75}$ was used, giving a corrected intensity of $I_{\text{corr}} = I/e^{-\tau(\lambda)}$. Plotting $\log(N_j/g_j)$ against E_j should give a straight line for low vibration levels and for a single characteristic excitation temperature in each pixel. If the value of A_k used to correct the line intensities from which the column density is calculated is wrong then the scatter of the points will increase. Our measurements are particularly sensitive to this because we have measured one H -band line (1 – 0 S(7) at 1.748 μm) which comes from an upper level close in energy to the upper level of two K -band lines (2 – 1 S(1) at 2.248 μm and 2 – 1 S(3) at 2.074 μm).

The value of A_k which minimised the scatter of the points was measured for each spatial pixel in the two brightest columns in the rebinned data-cube. It was found that the intensities of the 1 – 0 S(3) line and all the Q-branch lines other than the 1 – 0 Q(4) line were not consistent with any non-negative values of A_k . These lines were therefore assumed to be partly absorbed by the very narrow atmospheric lines which dominate the edges of the K -band window which, being spectrally unresolved, are not removed by dividing by the standard star. Once these lines were excluded the mean value of A_k over all the spatial pixels used was found to be $A_k = 0.7 \pm 0.1$, where the error on the derived value was estimated from the scatter of the values measured from one spatial pixel to another. The variation in the measurements appeared random, with no evidence for any systematic variation in extinction across the source. There was also no evidence of curvature in the N_j/g_j versus E_j plots, one of which is shown in Figure 6, though the absence of any points with upper energy levels between 8000 and 12000 K would make it hard to detect small deviations from a straight line. A curved line in this plot would provide evidence for non-LTE processes, such as would be seen for radiatively excited gas.

The line fluxes were measured at each spatial pixel in the rebinned data-cube and corrected for extinction using the extinction law described above. The value of N_j/g_j was then derived from each corrected line flux using Equation (1). The excitation temperature was measured by fitting Equation (2) to all of the measurements made at a single spatial pixel using a maximum likelihood method. When a single intensity is used there is a degeneracy between T and the constant of proportionality, causing the most likely value of the constant of proportionality to vary exponentially with T . For this reason Equation (2) was reformulated as

$$\frac{N_j}{g_j} = \exp\left(\frac{-E_j}{kT} + \alpha\right) \quad (3)$$

where α is the logarithm of the constant of proportionality.

The likelihood of a range of values of T and α was calculated for each measured line flux assuming a gaussian error distribution on the measurements of the line intensity and using a uniform prior probability density function for both parameters:

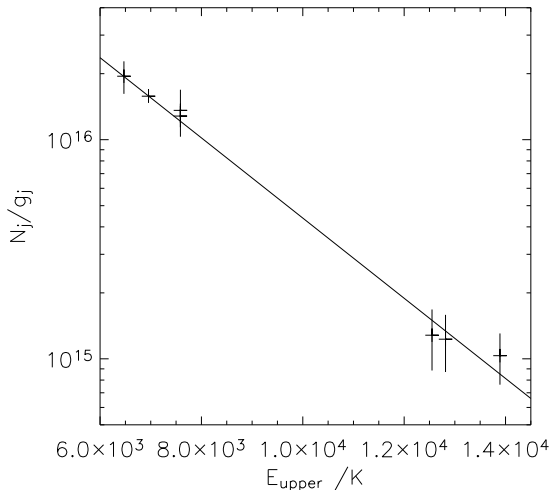


Figure 6. Plotting N_j/g_j against E_{upper} on a logarithmic scale gives a straight line after correcting for extinction using the extinction law described in the text. The solid line is given by Equation (3) using the maximum likelihood values of T and α . These measurements are taken from the $0.48\text{arcsec} \times 0.48$ arcsec region of the source marked 'd' Figure 4.

$$L_j(T, \alpha) \propto \frac{\exp[-(\delta/2\sigma)^2]}{\sigma\sqrt{2\pi}}. \quad (4)$$

In Equation (4) δ is the difference between the value of N_j/g_j derived from the measured intensity using Equation (1) and that calculated using Equation (3) and σ is the 1σ error on the measured value of N_j/g_j . When this is evaluated for a single spectral line there is a degeneracy between the two parameters, as shown in Figure 7a. The likelihood of the parameters using all the line fluxes is calculated by taking the product of all the individual likelihoods:

$$L(T, \alpha) = \prod_j L_j(T, \alpha) \quad (5)$$

This reduces the degeneracy (Figure 7b). The likelihood of each value of T , taking into account the uncertainty in α , can be calculated by marginalising the likelihood, or summing over all values of α to produce a one dimensional likelihood curve (Figure 8). The 68% confidence levels (the narrowest possible range of values of T to include 68% of the total area under the likelihood curve) were measured as an equivalent of 1σ error bars on a gaussian distribution.

These measurements were carried out along three 0.48 arcsec wide strips marked a, b and c on the image shown in Figure 4. The results are shown in Figure 9. The excitation temperature clearly increases from around 1800 K to (2840 ± 230) K (averaging over the most easterly pixel of all three slices) at what may be the shock front. In source A there also appears to be a decrease in excitation temperature of ~ 200 K to the right (east) in the image shown in Figure 4.

In Figure 4 it can be seen that both sources are brighter on the left (south) side than on the right. The temperatures measured in source A are approximately 200 K higher on the south edge of the IFU field than 1.5 arcsec to the north. We interpret this asymmetry in the north-south direction

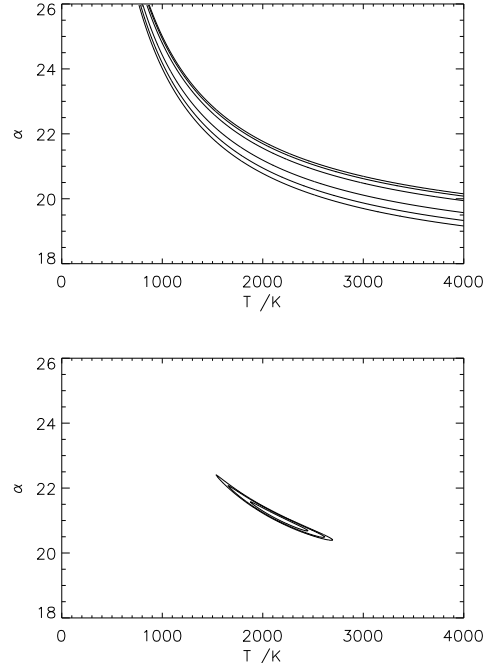


Figure 7. (a) The likelihood of the parameters T and α were evaluated for a single spatial pixel using the intensity of a single spectral line. (b) When other spectral lines are introduced the degeneracy is partly broken. On both plots the contours are at the 68%, 95% and 99% confidence levels, equivalent to 1σ , 2σ and 3σ error bars on a gaussian distribution.

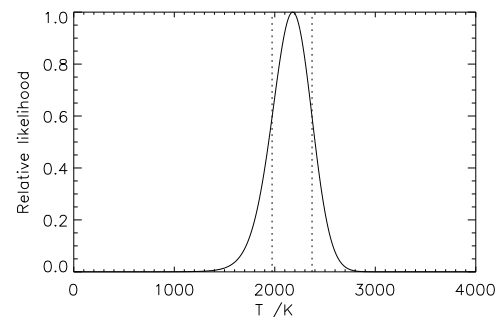


Figure 8. The marginal distribution of T can be obtained by integrating the distribution shown in Figure 7b over α . The likelihood shown here is normalised to have a maximum value of 1. The maximum likelihood value of T (2178 K in this case) and confidence intervals can be measured from this. The 68% confidence interval of $1973 - 2371$ K is shown by the dotted lines.

as supporting our interpretation of the H₂ emission being associated with a single outflow. If sources A and B are produced by a flow from west to east a symmetrical bow-shock would be expected. However, we cannot exclude the possibility that the asymmetry is produced by variations in density in the medium with which the outflow is interacting.

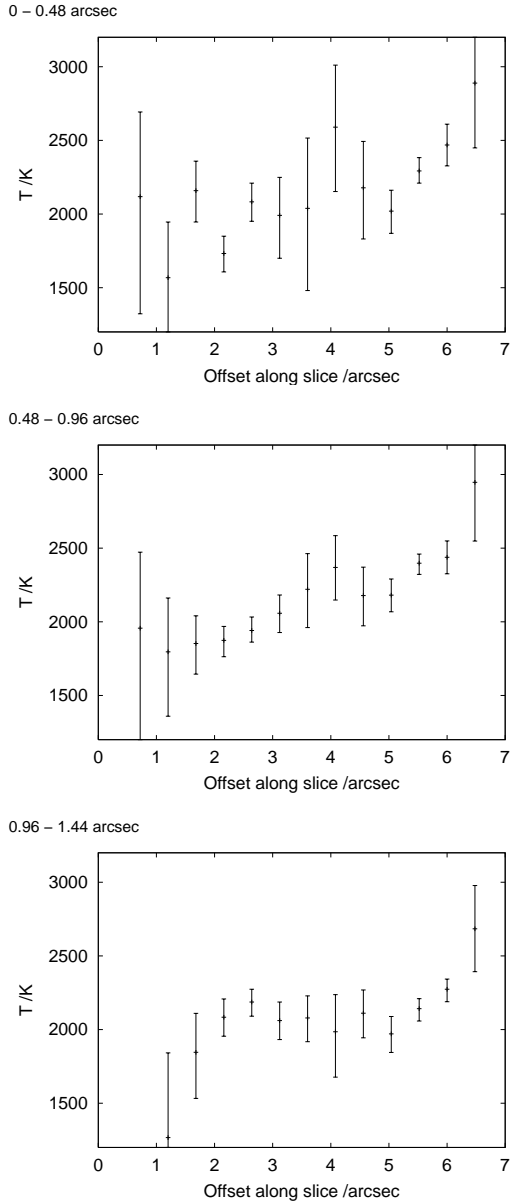


Figure 9. The temperature was measured along three 0.48 arcsec wide strips running west-east on the left of Figure 4. The points and error bars on these plots show the maximum likelihood value and 68% confidence interval on the value of T marginalised over α , as described in the text.

3.2.2 The Excitation Temperature of Sources C and D

The spectra of sources C and D are shown in Figure 3 and the relative line intensities in Table 2. Although the weather was non-photometric, both sources were observed simultaneously and the line ratios may be considered to be accurate, at the limit of the gaussian errors. The maximum likelihood analysis was repeated for C and D, giving an excitation temperature of 2730 K with 68% confidence levels of (2727 ± 227) K for source C and (2256 ± 250) K for source D, in each case averaged over the observed extent of the source.

3.2.3 Shock excitation

The properties of four classes of shocks were summarised by Davies et al. (2000):

(i) *fast J shock* ($100\text{--}300 \text{ km s}^{-1}$): hydrogen molecules are dissociated and reform producing a spectrum similar to that of UV fluorescence. The flux of Brackett- γ and H -band Fe II lines are comparable to the $1 - 0$ S(1) flux.

(ii) *slow J shock*: strong H₂ lines are produced and molecules are not dissociated. However, in normal ionization fractions, magnetic field strengths and gas densities, such shocks are expected to evolve into C-type shocks.

(iii) *fast C shock*: shock velocities of $\sim 40 \text{ km s}^{-1}$ heat the gas to $\sim 2000 \text{ K}$ or more (dependent on the velocity) producing strong H₂ lines.

(iv) *slow C shock*: peak temperature 300 K or less, resulting in very weak H₂ emission.

The absence of Brackett- γ emission from atomic hydrogen or Fe II lines and the excitation temperatures measured in all the sources ABCD leads us to suggest that the fast C shock model may be most appropriate. A maximum post-shock excitation temperature of (2840 ± 230) K would be produced by a shock velocity of $(37 \pm 3) \text{ km s}^{-1}$ in the models of Kaufman & Neufeld (1996). This would be consistent with the 29 km s^{-1} along the line of sight measured by Shepherd & Churchwell (1996b) when the uncertainty on the angle of incidence is taken into account. The temperatures measured in source A (offsets along the slice of between 4.5 and 6.5 arcsec) decrease with distance from the shock front. The C-shock models of Flower et al. (1996) predict a steady decrease in temperature over around 0.03 pc (2 arcsec at a distance of 3 kpc) behind the shock front, beyond which point the flux falls rapidly. This is consistent with what we see, though the proximity of source B and the uncertain geometry of the outflow inhibits more detailed comparison with the models. A more detailed analysis, including lines from higher vibrational levels examined as function of distance across the shock-front or high spectral resolution to explore the lines shapes would be required to allow us to draw stronger conclusions. Integral field spectroscopy is a technique that would lend itself readily to these observations.

4 SUMMARY

Mapping at high spatial resolution in the near-IR emission from H₂ we have directly observed outflow activity from one or more sources associated with G25.65+1.05. Long slit and integral field spectroscopy of the brightest sources show that they are excited by a shock. The measured excitation temperatures and absence of dissociation lead us to suggest that a C-shock with a shock velocity of $(37 \pm 3) \text{ km s}^{-1}$ may be responsible. Integral field spectra of a region containing two compact sources of H₂ emission showed a variation in excitation temperature with a maximum of 2800 K close to the shock front. The excitation temperature in the brighter of the two sources falls steadily over around 0.03 pc at which point the intensity decreases significantly, in agreement with the C-shock models of Flower et al. (1996).

Both the location of the brightest H₂ emission and

Table 2. Line ratios from the spectra of sources C and D.

Line	Ratio to 1-0 S(1)	
	Source C	Source D
1-0 S(1)	1	1
2-1 S(1)	0.15 ± 0.02	0.10 ± 0.04
1-0 S(0)	0.20 ± 0.05	0.36 ± 0.07
2-1 S(3)	0.22 ± 0.04	0.15 ± 0.05
1-0 S(2)	0.28 ± 0.08	0.52 ± 0.08

The ratio of line fluxes measured in the CGS4 spectra of sources C and D relative to the 1-0 S(1) line flux. The spectra were observed in cloudy conditions, so the absolute fluxes are unknown.

the derived shock speed are consistent with the excited H₂ tracing the same outflow as the CO emission detected by Shepherd & Churchwell (1996b).

We conclude that the most likely interpretation of these data is that the H₂ emission traces the full width of the outflow. In this case, the collimation factor of the outflow is ∼ 3, higher than the 1 to 1.8 often though to be typical of outflows from high mass stars.

The combination of near-infrared imaging and spectroscopy is a powerful method of revealing outflows in regions of high mass star formation. However, in the case of G25.65+1.05, the near-infrared data alone cannot determine unambiguously whether there are multiple or single outflows and driving sources. Supporting information may be sought in a number of ways. Higher resolution spectroscopy can help associated the emission with different outflows (see e.g. Davis et al. (2004) on IRAS18151-1208). High resolution imaging at wavelengths from 3-20microns and longer, such as is now possible from large ground based telescopes, may reveal additional deeply embedded sources.

The combination of high spatial resolution interferometric radio mapping with infrared imaging has been used successfully by e.g. Lee et al. (2001), Walsh et al. (2002) and Beuther et al. (2003) to examine the detailed structure and morphology of crowded regions containing multiple sources and outflows. G323.74-0.26 is revealed by the observations of Walsh et al. (2002) to contain both fluorescent H₂ emission from the HII region associated with this source and shocked H₂ emission from an outflow. Combining interferometric observations with infrared images of IRAS 19410+2336 Beuther et al. (2003) found that what had appeared in single dish maps to be two outflows was the combination of at least seven and possibly as many as nine separate outflows. It seems likely that similar results might be found in this region.

ACKNOWLEDGMENTS

The United Kingdom Infrared Telescope is operated by the Joint Astronomy Centre on behalf of the U.K. Particle Physics and Astronomy Research Council. The authors would like to thank the staff of UKIRT for their support in carrying out the observations presented here. We are grateful to the referee, Michael Burton, for his detailed comments

on the paper which have allowed us to improve it from the first submission.

REFERENCES

Beuther H., Schilke P., Sridharan T. K., Menten K. M., Walmsley C. M., Wyrowski F., 2002a, A&A, 383, 892
 Beuther H., Schilke P., Gueth F., McCaughrean M., Anderson M., Sridharan T., Menten K., 2002b, A&A, 387, 931
 Beuther H., Schilke P., Stanke T., 2003, A&A
 Bronfman L., Nyman L.-A., May J., 1996, A&AS, 115, 81
 Davies R., Ward M., Sugai H., 2000, ApJ, 535, 735
 Davis C. J., Varricatt W. P., Todd S. P., Ramsay Howat S. K., 2004, A&A, 425, 981
 Egan M. P., Price S. D., Moshir M. M., Cohen M., Tedesco E., 1999, NASA STI/Recon Technical Report N, 14854
 Faúndez, S., Bronfman, L., Garay, G., Chini, R., Nyman, L.-Å., & May, J. 2004, A&A, 426, 97
 Flower D. R., Pineau des Forêts G., Field D., May P. W., 1996, MNRAS, 280, 447
 Garay G., Lizano S., 1999, PASP, 111, 1049
 Gibb E. L., Whittet D. C. B., Boogert A. C. A., Tielens A. G. G. M., 2004, ApJS, 151, 35
 Hill, T., Burton, M. G., Minier, V., Thompson, M. A., Walsh, A. J., Hunt-Cunningham, M., & Garay, G. 2005, MNRAS, 363, 405
 Hunter T. R., Churchwell E., Watson C., Cox P., Benford D. J., Roelfsema P. R., 2000, AJ, 119, 2711
 Kaufman M. J., Neufeld D. A., 1996, ApJ, 456, 611
 Kurtz S., Churchwell E., Wood D. O. S., 1994, ApJS, 91, 659
 Lee, J.-K., Walsh, A. J., Burton, M. G., & Ashley, M. C. B. 2001, MNRAS, 324, 1102
 Molinari S., Brand J., Cesaroni R., Palla F., 1996, Astron.Astrophys., 308, 573
 Molinari S., Brand J., Cesaroni R., Palla F., Palumbo G. G. C., 1998, Astron.Astrophys., 336, 339
 Mountain C. M., Robertson D. J., Lee T. J., Wade R., 1990, in Instrumentation in astronomy VII; Proceedings of the Meeting, Tucson, AZ, Feb. 13-17, 1990 (A91-29601 11-35). Bellingham, WA, Society of Photo-Optical Instrumentation Engineers, 1990, p. 25-33. Previously announced in

STAR as N90-19165. An advanced cooled grating spectrometer for UKIRT. pp 25–33

Palla F., Brand J., Comoretto G., Felli M., Cesaroni R., 1991, *Astron. Astrophys.*, 246, 249

Ramsay Howat S. K., Ellis M. A., Gostick D. C., Hastings P. R., Strachan M., Wells M., 2000, in *Proc. SPIE Vol. 4008*, p. 1067-1075, Optical and IR Telescope Instrumentation and Detectors, Masanori Iye; Alan F. Moorwood; Eds. Integration and testing of the UKIRT imaging spectrometer (UIST). pp 1067–1075

Richer J., Shepherd D., Cabrit S., Bachiller R., Churchwell E., 2000, in *Protostars and Planets IV Molecular outflows from young stellar objects*. Arizona, pp 867–894

Ridge N. A., Moore T. J. T., 2001, *A&A*, 378, 495

Roche P. F., Lucas P. W., Mackay C. D., Ettedgui-Atad E., Hastings P. R., Bridger A., Rees N. P., Leggett S. K., Davis C., Holmes A. R., Handford T., 2003, in *Instrument Design and Performance for Optical/Infrared Ground-based Telescopes*. Edited by Iye, Masanori; Moorwood, Alan F. M. *Proceedings of the SPIE*, Volume 4841, pp. 901-912 (2003). UFTI: the 0.8 - 2.5 μ m fast track imager for the UK infrared telescope. pp 901–912

Shepherd D. S., Churchwell E., 1996b, *ApJ*, 472, 225

Shepherd D. S., Churchwell E., 1996a, *ApJ*, 457, 267

Sridharan T. K., Beuther H., Schilke P., Menten K. M., Wyrowski F., 2002, *Ap.J.*, 566, 931

Sternberg A., Dalgarno A., 1989, *ApJ*, 338, 197

Szymczak M., Hrynek G., Kus A. J., 2000, *A&AS*, 143, 269

Todd S. P., Wells M., Ramsay Howat S. K., Hastings P. R., 2002, in E. Atad-Ettedgui D'Odorico S., eds, *Specialized optical developments in astronomy No. 4842* in *Proc. SPIE*, A cryogenic image slicing IFU for UKIRT – manufacture, alignment, laboratory testing and data reduction. pp 151–161

Walsh, A. J., Burton, M. G., Hyland, A. R., & Robinson, G. 1999, *MNRAS*, 309, 905

Walsh, A. J., Lee, J.-K., & Burton, M. G. 2002, *MNRAS*, 329, 475

Walsh A. J., Macdonald G. H., Alvey N. D. S., Burton M. G., Lee J.-K., 2003, *A&A*, 410, 597

Zavagno A., Deharveng L., Nadeau D., Caplan J., 2002, *A&A*, 394, 225

Zhang Q., Hunter T. R., Brand J., Sridharan T. K., Molinari S., Kramer M. A., Cesaroni R., 2001, *ApJ*, 552, L167